



Design and mathematical modeling of polymeric phases to obtain controlled microporosity materials by 3D printing

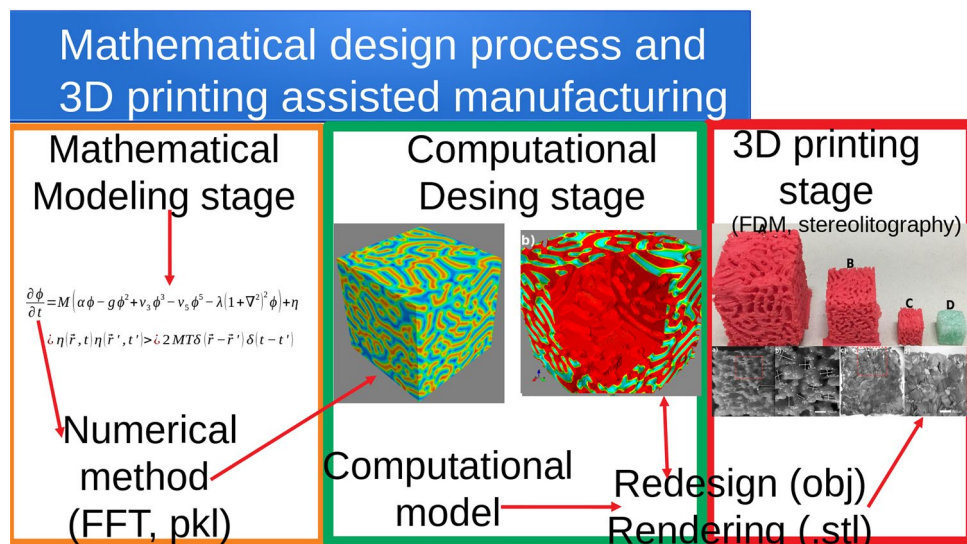
Marco A. Morales¹ · Sinhue Ruiz-Salgado¹ · Ricardo Agustín-Serrano² · Benito Zenteno-Mateo³ · José I. Rodríguez-Mora³

Received: 7 October 2021 / Accepted: 11 March 2023 / Published online: 14 April 2023
© The Author(s), under exclusive licence to Springer Nature Switzerland AG 2023

Abstract

A new method named implicit pseudo-spectral arrays (IPSA) was developed to obtain the numerical solution and plot it as a three-dimensional (3D) pattern. These results were used to elaborate the computational simulation of the spatio-temporal dynamics of the Swift–Hohenberg equation (SHE) of quintic order. Numerical solutions are employed as complex 3D computational models (computer-aided design files), which were studied and analyzed to generate a new method named "mathematical design process and 3D printing-assisted manufacturing (MDP-3DPAM)". This new technique is a new way to create porous polymeric materials through a controlled mathematical shape with pore size distribution and microstructure modulated by software parameters. Another advantage of this design process is its efficient computational computation time and various 3D printing methods available, such as: fused deposition modeling and UV-laser-assisted stereo-lithography. In this work, both techniques were used in the printing of porous materials. This work establishes a method for controlling pore size distribution through mathematical modeling and subsequent printing.

Graphical abstract



Keywords 3D Simulation · Modeling · Additive manufacture · Stereolithographic · Microporous materials · Computational design

✉ Marco A. Morales
spinor70@yahoo.com.mx

Extended author information available on the last page of the article

1 Introduction

Processing techniques for porous materials have great potential in applications ranging from nanoscience to catalysis and photo-catalysis, separation processes, energy conversion, and storage. The applications of these porous materials take place according to the hierarchy of the porous structure due to their pore size distribution and morphology [1]. Therefore, pore size control, microstructure, chemical composition, and morphology are the main control variables in their synthesis and processing. Advance research has not yet reached the level of complexity of porous natural materials (such as the butterfly wood, leaf, macaw feather, grass stem, kelp, coral, cotton, human bone, cuttlefish bone, and the sponge) with hierarchically porous structure made of interconnected pores with different lengths ranging from micropores (<2 nm), mesopores (2–50 nm) to macropores (> 50 nm). Furthermore, the morphology of these examples of porous natural materials can have multi-porosity (a combination of two or more types of porosity) [1]. All these porous structures are challenging to reproduce and control. To date, there is no method to manufacture and control pore size distribution effectively for synthetic materials.

On the other hand, tridimensional (3D) printing (or additive manufacturing) [2] offers advantages, such as high precision, low cost, and customized geometry at the microporosity scale. Currently, 3D printing technology, such as new composite materials based on high-performance engineering thermoplastics (ET), provides a basis for increased thermal and mechanical performances to address the limitations of extrusion 3D printing [3]. Also, modifications to the 3D printing techniques allow obtaining diverse geometries of cellular continuous fiber-reinforced composites [4]. Another new method, roll-to-roll 3D printing, allows a faster and more massive commercial production scale of organic solar cells based on polymer/perovskite [5]. In addition, the other techniques have emerged apart from conventional additive manufacturing (or fused deposition modeling) like new laser sintering or stereo-lithography (among others) [6], doing possible new membranes for wastewater treatments, and separation of ionic species from pharmaceutical products [7].

Mathematical models in recent studies with SHE solved numerically in two and three dimensions through new numerical methods, such as first- and second-order semi-analytical Fourier spectral methods [15], meshless local collocation method [16], and unconditionally stable semi-implicit time discretization [17], minimization method of SHE functional [18]. These methods are computationally cheap and have a high-order time accuracy performance, which is compatible with the "mathematical design process, and 3D printing-assisted manufacturing" (explained in detail below). The numerical solution from these methods,

obtained by computational simulation, presents the following morphologies: planar lamellar phase [15, 17], disordered nucleus phase [16], twisted lamellar phase [17], labyrinths [18], hexagonal [17, 18], and body-centered cubic (bcc) [18] phases. In contrast, in past studies [15, 19, 20], the SHE has been employed for explaining the pattern formation in hydrodynamic systems [19], Rayleigh–Bénard convection [21], and two labyrinths [22], isotropic, nematic, and smectic phases [20] in diblock copolymers. Furthermore, extended models of this equation have been proposed for research in that conditions emerge the pinning dynamics [23–25] and anisotropy [26] of hexagonal [23, 24], strips [25, 26], and labyrinths [27] phases, respectively.

Likewise, thanks to the various 3D printing techniques, prostheses, bone fillings, and scaffolds are manufactured for the tissue engineering area [8]. Fused deposition modeling refinement techniques allow generating of recyclable, lightweight polymeric structures or devices with hierarchical architectures, complex geometries of improved rigidity, and toughness due to bottom-up molecular control over the orientation of the injected polymer [9]. In addition, it is possible to produce hydrogel scaffolds based on dextran oxide/gelatin/cellulose nanoparticles for tissue repair [10] or composite scaffolds for bone regeneration based on polylactic acid due to their improved bio-functionality [11]. Composite scaffolds for bone regeneration based on polylactic acid due to its improved bio-functionality, either by 3D conventional additive manufacturing to obtain scaffolds with the morphology of bone tissue with sodium-alginate/hydroxyapatite coating [12] or by direct extrusion as a filament of a nanocomposite material based on graphite nanoplatelets/PLA/L-Arginine [13]. The novel inverse 3D printing method's application allows scaffolds with a rectangular distribution of uniform porosity of β -tricalcium phosphate, also for bone regeneration [14].

Even more, this work addresses the SHE extended again with the stabilizing quintic and destabilizing cubic terms [28–32] to obtain their bifurcations analysis [28, 31, 32] and the numerical solution in 3D [28, 29] to perform a porous simulated and controlled structure. The Materials and methods section proposes a new method of the mathematical design process and 3D printing-assisted manufacturing (MDP-3DPAM). In the "Numerical experiments: 3D computational simulation" section, the results of 3D numerical solutions of the quantic SHE models are presented. And, the section "Description of complex 3D computational models" is described and compared with natural systems. The porous materials' prototypes obtained by fused deposition modeling and stereo-lithography UV-laser assisted are found in the next section. Finally, in the last sections, a discussion and conclusions of this paper are placed, and appendixes related to 3D computer simulations and 3D printing are presented.

2 Materials and methods

2.1 Materials

A 32 GB RAM computer running on the Kubuntu operating system achieved the numerical simulation patterns. Python 2.7 and its scientific extensions, such as NumPy, matplotlib, and mlab, were used [33]. The graphics of the numerical solution obtained were drawn in Mayavi in its second version [34]. A TEVO LITTLE MONSTER 3D with a 0.4 resolution nozzle and a Creality 3D id-002r printer achieved porous polymeric materials' creation with PLA red color filament from 3D SOLUTECH and ELEGOO photopolymer transparent resin.

Hereinafter, the proposed method that allows obtaining polymeric materials with controlled porosity is described. This method is constituted by three stages (*Mathematical modeling, Computational design, and 3D printing stages*), which is named as mathematical design process and 3D printing assisted manufacturing (MDP-3DPAM), see Fig. 1.

2.2 Mathematical modeling stage: IPSA method outline

The numerical method employed for solving Eq. (A1) of Appendix A in the supporting information document is the implicit pseudo-spectral method described in [35], which is extended easily to 3D space. The spatial domain (discretized by a mesh of $N_x \times N_y \times N_z$ nodes) of this equation is periodic in all directions (x, y, z), which is an approach that applies the discrete Fourier transform on the solution of the scalar field $\phi(\vec{r}, t)$. This method based on such discrete transforms provides optimal accuracy in that the rate of convergence for suitably smooth solutions is faster than any power of the mesh of $N_x \times N_y \times N_z$ nodes. The calculus of nonlinear terms is integrated using an exponential propagation procedure described in detail below, with the nonlinear terms handled explicitly, while a fully implicit approach is constructed. To better approximate, these terms can be treated as a linear

system of differential equations modified by a nonlinear forcing term. The nonlinear terms are integrated by a predictor–corrector method. It can be shown that the overall technique is second-order accurate in time step bigger than with the finite difference methods. The implicit pseudo-spectral method is extended to array algorithms as follows. It is well known as the Fourier transform changes a gridded cubic space (GCS) with a mesh of $N_x \times N_y \times N_z$ nodes in a Fourier transformed space (FTS) with $(q_x)_i \times (q_y)_j \times (q_z)_k$ nodes number, such that: $-\left(\frac{N_x}{2} - 1\right) \leq i \leq N_x/2, -\left(\frac{N_y}{2} - 1\right) \leq j \leq N_y/2$ and $-\left(\frac{N_z}{2} - 1\right) \leq k \leq N_z/2$. The equations that define the coordinates of each point on the GCS mesh are: $x_i = \frac{(i-1)L_x}{N_x}, i = 1, \dots, N_x, y_j = \frac{(j-1)L_y}{N_y}, j = 1, \dots, N_y, z_k = \frac{(k-1)L_z}{N_z}, k = 1, \dots, N_z$, where L_x, L_y, L_x , and L_z the spatial region dimensions in the x, y , and z directions. Furthermore, the points on the FTS mesh are such that: $(q_x)_i = 2\pi i/L_x, (q_y)_j = 2\pi j/L_y, (q_z)_k = 2\pi k/L_z$. An initial condition array from GCS was developed and then applied the numerical method described in Sect. 3.2 under the array of FTS of $(q_x)_i \times (q_y)_j \times (q_z)_k$ nodes. The "NumPy" library for python distribution [33] allows evaluating simultaneously the implicit pseudo-spectral algorithm method in the FTS matrix utilizing an initial conditions matrix seed, in which the discrete Fourier transform is applied. NumPy library contains the FFT.py module that is a simple interface to the FFTPACK FORTRAN library, which is a powerful standard library for doing fast Fourier transforms of real and complex data sets.

As implementation example of this stage is solved numerically the spatial–temporal behavior of the fifth-order SHE (given by Eq. (A1) in Appendix A of support information). This equation is solved using the ISPA method developed in the previous section. Their numerical solution of Eq. (A4) was obtained by discretizing a square grid of mesh size $\Delta x = 0.5$ with $128 \times 128 \times 128$ nodes, where periodic boundary conditions had been used. The values of control parameters are selected in Table B1 of Appendix B of the supporting information document. The numerical solution can be graphed in the Cartesian space, and each data value can be assigned with a different color. This arrangement of the numerical data has a specific morphology in the three-dimensional space, which we name as 3D pattern that has a characteristic wavelength q_0 . Based on the stability analysis of Appendix C of the supporting information document, we selected the critical wavenumber $q_0 = 2\pi/\lambda_0$ where wavelength $\lambda_0 = 2\pi\Delta x$, such that $q_c = 1$. The temporal evolution of the system is performed with a time step $\Delta t = 0.1$ and $T = t\Delta t$ adimensional time units with t iterations numbers. For each obtained 3D patterns are employed, initial random conditions. The initial conditions for $\phi(\vec{r}, t)$ are random

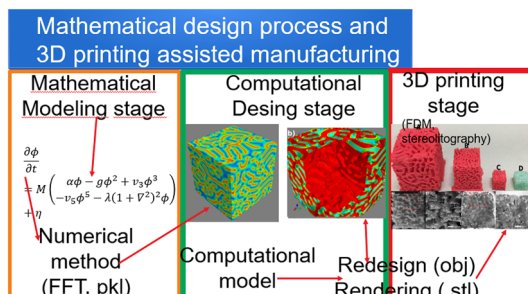


Fig. 1 Representative diagram of the three concatenated stages that constitute the method MDP-3DPAM

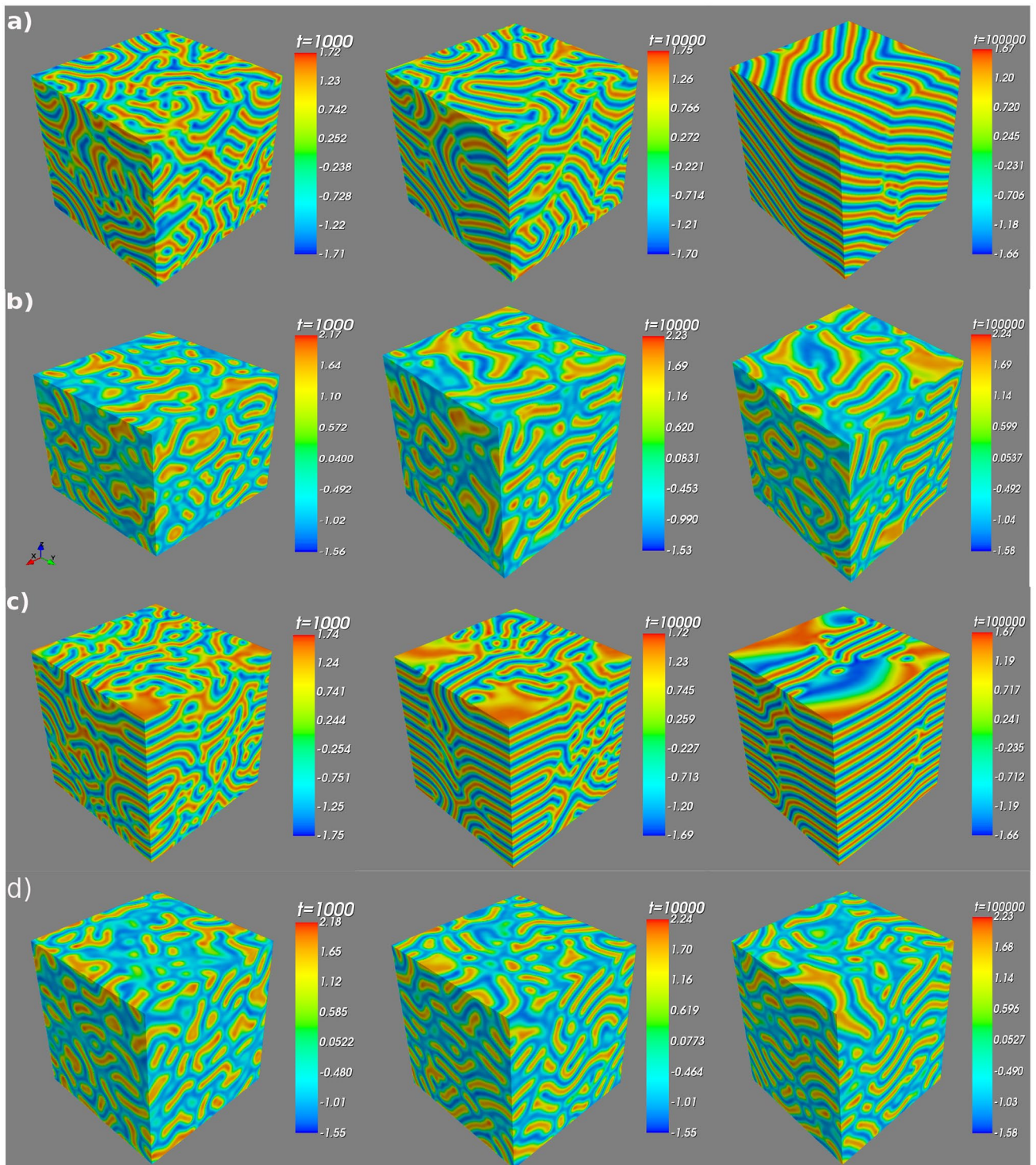


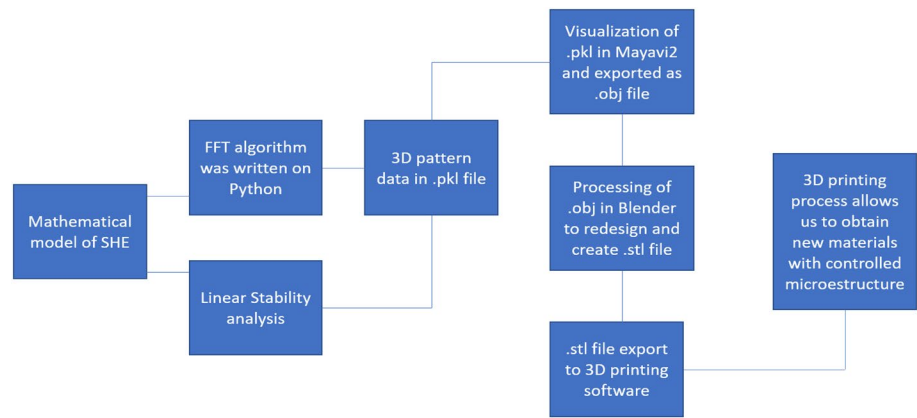
Fig. 2 Spatial–temporal dynamics solutions of fifth-order SHE. Where t represents the iterations steps number, and the values of control parameters are localized in Table B1 of Appendix B in the supporting information document

variables with values in the range $[-\sqrt{|\alpha|}, \sqrt{|\alpha|}]$ and a Gaussian distribution of zero averages and variance $\langle \phi^2 \rangle = 0.1$. For the observation of the 3D patterns, see Fig. 2.

2.3 Computational design stage

The method to create a computer-aided design (CAD) file from polymeric material resulting in a controlled pore size distribution object; Fig. 3 shows the process for developing

Fig. 3 Workflow diagram of the mathematical design process and 3D printing-assisted manufacturing (MDP-3DPAM) in generating 3D printed porous materials with controlled microstructure. The chart should be read from left to right. The linear stability analysis was done to identify points of interest for study pattern formation (see also Graphical Abstract)



materials with controlled microstructure and starting with the 3D pattern numerical solution obtained from the IPSAM algorithm based on SHE of quantic order, which is programmed in Python shell. If the reader wants to review a detailed description of the mathematical model, as well as the numerical method of the fast Fourier transform (FFT) to obtain a numerical solution for the fifth-order SHE, you can see the supporting information document (Appendix A). This 3D numerical solution is then analyzed on its.pkl file format by Mayavi2 software to obtain a.obj file so it can be afterward translated into standard triangle language

extension (.stl). At this stage, the pore size is controlled as much as desired (see, for example, Fig. 4).

2.4 3D printing stage

The 3D models can be exported to any printer (Repeater Host in this case) software code generator for the final processing step, which also allows controlling the size and printing parameters for the impression in the materials analyzed in the next section. PLA material heated to 210 °C was used to achieve the final structures while printing by additive manufacturer, while UV photopolymer

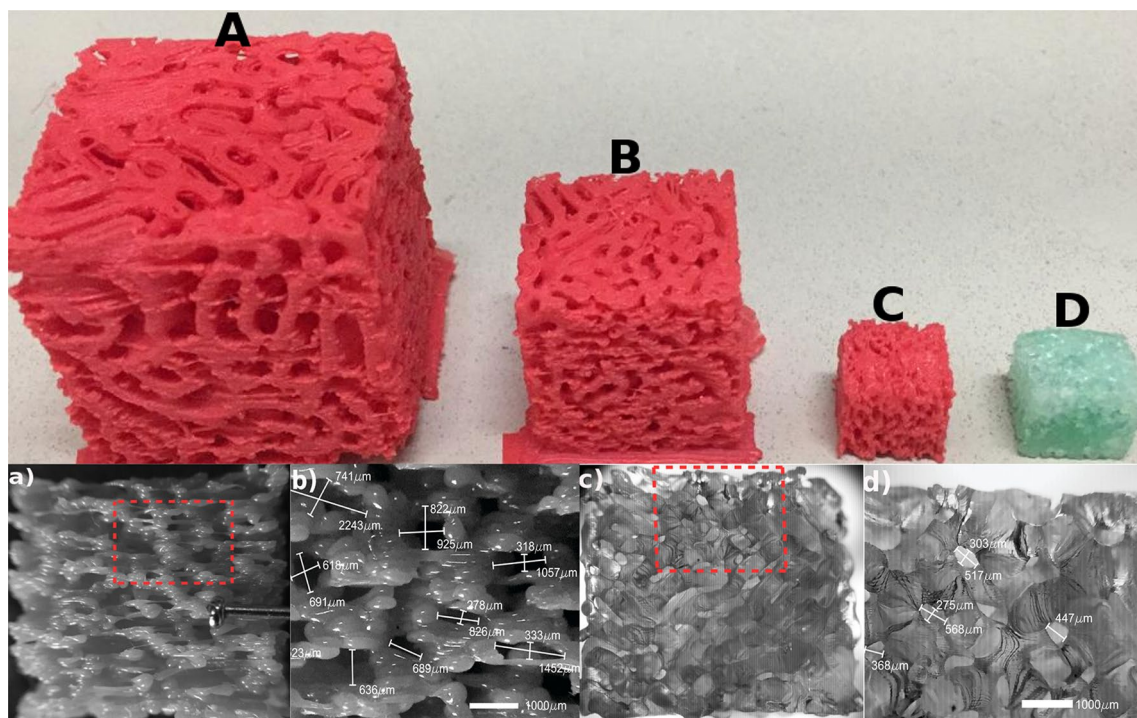


Fig. 4 Microporous polymeric materials obtained by additive injection (patterns A–C) and stereo-lithography (pattern D) 3D printing. The below panel is shown in a and c a face of patterns C and D,

respectively. Images b) and d) obtained by stereoscopic microscopy are zooms of a face section of C and D patterns

resin was used to accomplish the other printing method known as stereo-lithography. Extruding different polymers allows the creation of solid structures with complex mechanical properties and controlled pore size distribution. The 3D printing process using mathematical models to design the pattern [12, 22] is an entirely new method to design and create new advanced materials.

3 Results

3.1 Numerical experiments: a 3D computational simulation

Obtained patterns from the numerical simulation are like the ones already reported in the literature. Figure 2 shows a phase change from isotropic to neumatic when turning on a control parameter ($g = 2$) which is like the behavior demonstrated by the third-order SH model [19–21, 36, 37]. Other behaviors like the numerical experiments reported in references [18, 22, 27] are consistent with the labyrinth phase shown in Fig. 2a. Moreover, when the control parameter g is turned on, there is a symmetry breaking that manifests itself in a pattern with island morphology like the patterns of the Ginzburg–Landau equation reported in [37–40]. This behavior is analogous to that reported in the typical SH model of quantic order when changing a control parameter to obtain a hexagonal phase from the gut phases [17, 18, 23–27]. A complete and detailed study of phase transitions and space–time dynamics is a motive for future studies. The linear stability analysis is presented in Appendix C of the supporting information document. Its study allows the selection of the control parameter values that are important for the development of this research.

3.2 Description of complex 3D computational models

Some 3D structure patterns are obtained by computational simulation from the quintic SHE and can be used for the study of porous materials models in a similar way as reported in [41–43], which allows the processing of new porous polymeric materials as it will be shown in the next section. Figure 2a–c exhibits two phases separated into two 3D structures that are negative and positive phases from the original simulated pattern of Fig. 2a. The positive phase morphology from the central image of Fig. 5a is very similar to the zeolite 3D structure of the perovskite. In contrast, the 3D structure from the central image of Fig. 5b is a biomimetic structure like the extracellular matrix from trabecular bone obtained by the method reported in other works [12, 22, 44, 45].

To finish this section, there is a structure comparison of the positive phase from the central image of Fig. 5c with the fingerprint photo of a real finger. Both 3D morphologies are similar in the shape of the grooves. This is consistent qualitatively with the slow dynamics of the skin of fingers and hands in the human body. The images from the third column on the right are natural structures obtained by SEM micrograph: (a) coral microstructure, (b) bone extracellular matrix (see [44, 45]), and (c) a fingerprint photo from the index finger.

3.3 Results of fused deposition modeling and stereo-lithography UV-laser assisted

Objects were printed in polylactic acid (PLA) filament, a thermoplastic polymer operated around 215 °C, but they are not limited only to this polymer; any polymer can be printed under certain conditions. The porosity of these materials can be directly controlled by varying the parameter α , chosen to simulate (see Table B1), which is related to the pattern morphology. In the second place, scaling this morphology in Blender to finally obtain a specific porous pattern with different pore size distributions and specific surface area due to the size scaling process. Instead of porous chemical composition structure dependence, as is shown in Fig. 4. These figures show the microporosity of the porous polymeric materials (see Fig. 4c and d) that were scaled to an eighth of their original size (see Fig. 4A), obtained by fused deposition modeling [Fig. 4A–C] and stereo-lithography UV-laser assisted [Fig. 4D, c and d], respectively.

The manufacture of polymeric porous materials by molten deposition modeling (or fabrication by filament fused) is realized to compare with stereolithographic 3D printing. Another advantage of using this 3D printing technique probes the universality of the new method proposed in this work: the mathematical design process and 3D printing-assisted manufacturing.

By direct observation, comparing Fig. 4b with Fig. 4d can be concluded that the macropores of the PLA porous material have an extensive size range of 600–1200 μm with bad definition, while the macropores of the resin have a larger size in a range of 300–500 μm . It can conclude that the 3D printing by stereo-lithography UV-laser assisted allows a better control to obtain a microporosity with the morphology of Fig. 4b. These polymeric matrices can bio-mimic the extracellular anisotropic matrix from the coronal cross-section of long trabecular bone [44, 45], under the chemical treatment of [12] in which the composite biomaterials are presented as promising scaffolds that can be degraded and absorbed by the human body, without showing biological rejection. Wolf's law [44, 45] will be subject to future studies to determine that the polymer morphology of Fig. 4c fulfills a hierarchical structure from the human proximal

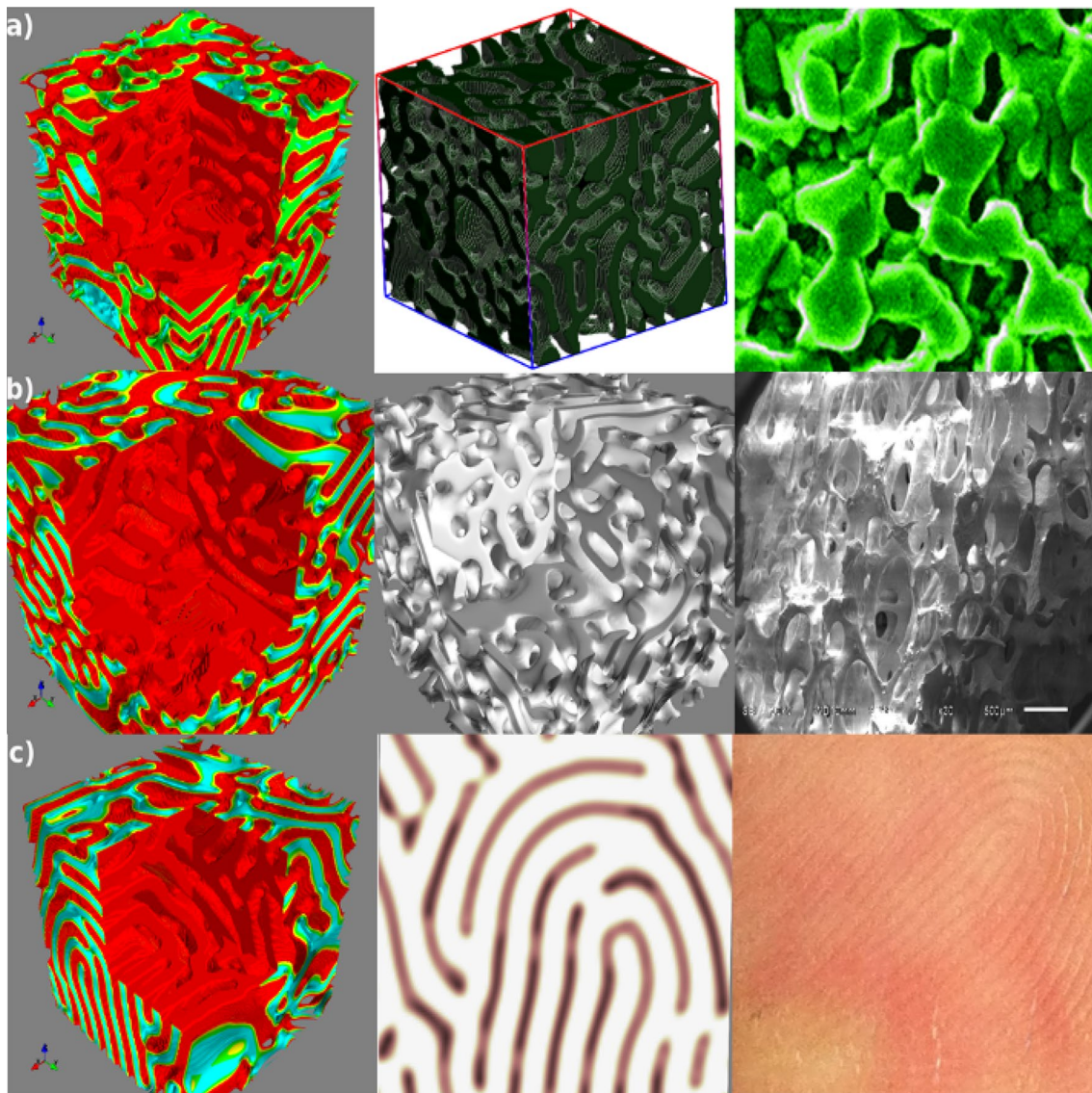


Fig. 5 The negative and positive phases from the computational simulations are the first and second columns from left to right: **a**, **b**, and **c** colored with red, light-green, dark green, and white, respectively

femur (e.g.). Figure 1D of Appendix D in the document of Supporting Information shows the open-pore system in the interior of the polymeric porous cube obtained by 3D printing. And the relationship between the print size and the pore size on one side of the 3D pattern, is presented in Appendix E, Fig. 1E (document of Supporting Information).

From the advancement of 3D printing as additive manufacturing (fabrication by fused filament), today, news techniques have emerged as Digital Light Processing (DLP) which allows printing facial prostheses [46] and meniscus implants for a knee in bland materials [47, 48] as the

medical-grade silicone. Even more, using a machine learning algorithm [49] can optimize the processing of silicone materials, the formulation, and the central processing variables to manufacture bone scaffolds as polymeric porous materials with sodium-alginate/hydroxyapatite coating or silicone/hydroxyapatite composite materials. This hierarchical machine learning has been employed recently to determine the purity, composition, structure, dimensions, and mechanical properties of silicone implants that are affected using a 3D printer by DLP [49].

4 Discussion

A recent study [50] proposed an efficient numerical method for arbitrary-shaped porous structure generation for 3D printing, which is like published in the references [12, 22] (although it employed another numerical method). Nevertheless, in our work, scientific is proposed a new plan of computational design and manufacture of porous polymeric materials with controlled macroporosity. Although both works are similar concerning obtaining porous materials from mathematical models, our work proposes a general method that allows the use of any numerical method and 3D printing technique: the mathematical design process and 3D printing-assisted manufacturing MDP-3DPAM. For example, the new way proposed can be applied to the numerical methods employed in the references [12, 22]. While the manufacturing technique presented in the relation [50] is dependent on their numerical way: Fourier Fast Transform. This numerical method also is employed in the procedure MDP-3DPAM proposed, but with a subtle difference: in our process, the FFT is implemented in python in matrix form (objects "array"). Note that the Swift–Hohenberg equation cannot be solved by the FFT method proposed in [50]. Another fundamental difference between both works is that our proposed method allows control of porosity through the computational design stage, which can determine the pore size through the design and type of 3D printing. In the section "Results of fused deposition modeling and stereolithographic UV-laser assisted," the pore size is shown according to the 3D printing technique used to manufacture the porous material. Finally, the method for obtaining porous polymeric materials proposed in reference [50] has a single stage. In contrast, the method proposed in this paper consists of three interconnected phases: mathematical modeling, computational design, and 3D printing. In future work, they would be using the shape memory effect materials for 3D printing that can have various applications as cellular structure composite with a novel continuous fiber-reinforced printing path [4, 51].

5 Conclusions

The quintic order Swift–Hohenberg equation presented here is a more general equation than those reported in the references of this work, because it has been extended to a 3D model. Besides, its numerical solution is obtained in the three-dimensional space by a pseudo-spectral implicit method. The numerical method of the IPSA has been successfully applied to solve in the three-dimensional space the Swift–Hohenberg equation of quantic order with the FFT

method employing an algorithm that is easy to reproduce and that also poses an acceptable calculation time.

The dynamics of the 3D simulations obtained by the numerical solution from the IPSA method can be well used to explain nonlinear behaviors that are far from equilibrium. Besides, it allows defying the underlying mechanism in the polymeric materials area. Some examples of this are the diblock copolymer blend phases and new computational models able to generate controlled 3D porous microstructures.

All the above has ended in a new methodology focused on implementing the numerical solutions as computational models able to generate controlled 3D microporous structures to process new polymeric porous materials like the ones that have been reported in [12, 22, 44, 45]. The advantage of this methodology is the pore size distribution control through the mathematical design process and assisted by 3D printing their easy implementation by different techniques: fused deposition modeling and stereo-lithography UV-laser assisted. Even this proposed method has universal properties as it is compatible with other numerical methods [16–18] and other 3D printing techniques [2–7].

Supplementary Information The online version contains supplementary material available at <https://doi.org/10.1007/s40964-023-00437-4>.

Acknowledgements Thanks to the financial support from PROMEP-SEP, Mexico (Grant No. BUAP-PTC-581, 511-6/17-8017) in the realization of this work.

Funding The work of Benito Zenteno-Mateo was supported by the Secretaría de Educación Pública, México, under Grant No. BUAP-PTC-581.

Data availability The authors declare that the data supporting the findings of this study are available within the paper and its supplementary information file.

Declarations

Conflict of interest The authors of this work declare that there is no conflict of interest.

References

1. Yang XY, Chen LH, Li Y, Rooke JC, Sanchez C, Su BL (2017) Hierarchically porous materials: synthesis strategies and structure design. *Chem Soc Rev* 46:481. <https://doi.org/10.1039/C6CS90043G>
2. Gibson I, Rosen D, Stucker B (2015) Additive manufacturing technologies: 3D printing, rapid prototyping, and direct digital manufacturing, 2nd edn. Springer, New York
3. Picard M, Mohanty AK, Misra M (2020) (2020) Recent advances in additive manufacturing of engineering thermoplastics: challenges and opportunities. *RSC Adv* 10:36058. <https://doi.org/10.1039/D0RA04857G>

4. Dong K, Ke H, Panahi-Sarmad M, Yang T, Huang X, Xiao X (2021) Mechanical properties and shape memory effect of 4D printed cellular structure composite with a novel continuous fiber-reinforced printing path. *Mater Des* 198:109303. <https://doi.org/10.1016/j.matdes.2020.109303>
5. Gusain A, Aparna T, Sabu T (2020) Roll-to-roll printing of polymer and perovskite solar cells: compatible materials and processes. *J Mater Sci* 55:13440. <https://doi.org/10.1007/s10853-020-04883-1>
6. Wang X, Jiang M, Zhou Z, Gou J, Hui D (2017) 3D printing of polymer matrix composites: a review and prospective. *Compos B* 110:442. <https://doi.org/10.1016/j.compositesb.2016.11.034>
7. Seo J, Kushner DI, Hickner MA (2016) 3D printing of micropatterned anion exchange membranes. *ACS Appl Mater Interfaces* 8:16656. <https://doi.org/10.1021/acsami.6b03455>
8. Kang HW, Lee SJ, Ko IK, Kengla C, Yoo JJ, Atala A (2016) A 3D bioprinting system to produce human-scale tissue constructs with structural integrity. *Nat Biotechnol* 34:312. <https://doi.org/10.1038/nbt.3413>
9. Gantenbein S, Masania K, Woigk W, Sesseg JPW, Tervoort TA (2018) Three-dimensional printing of hierarchical liquid-crystal-polymer structures. *Nature* 561:226. <https://doi.org/10.1038/s41586-018-0474-7>
10. Jiang Y, Zhou J, Shi H, Zhang Q, Feng C, Xv X (2020) Preparation of cellulose nanocrystal/oxidized dextran/gelatin (CNC/OD/GEL) hydrogels and fabrication of a CNC/OD/GEL scaffold by 3D printing. *J Mater Sci* 55:2618. <https://doi.org/10.1007/s10853-019-04186-0>
11. Donate R, Monzón M, Alemán ME (2020) Additive manufacturing of PLA-based scaffolds intended for bone regeneration and strategies to improve their biological properties. *E-Polymers* 20:571. <https://doi.org/10.1515/epoly-2020-0046>
12. Fernández-Cervantes I, Morales MA, Agustín-Serrano R, Cardenas-García M, Pérez-Luna PV, Arroyo-Reyes BL, Maldonado-García A (2019) Polylactic acid/sodium alginate/hydroxyapatite composite scaffolds with trabecular tissue morphology designed by a bone remodeling model using 3D printing. *J Mater Sci* 54:9478. <https://doi.org/10.1007/s10853-019-03537-1>
13. Wang Y, Lei M, Wei Q, Wang Y, Zhang J, Guo Y, Saroia J (2020) 3D printing biocompatible L-Arg/GNPs/PLA nanocomposites with enhanced mechanical property and thermal stability. *J Mater Sci* 55:5064. <https://doi.org/10.1007/s10853-020-04353-8>
14. Seidenstuecker M, Lange S, Esslinger S, Latorre SH, Krastev R, Gadow R, Bernstein A (2019) Inversely 3D-Printed β -TCP Scaffolds for bone replacement. *Materials* 12:3417. <https://doi.org/10.3390/ma12203417>
15. Lee HG (2017) A semi-analytical Fourier spectral method for the Swift-Hohenberg equation. *Comput Math Appl* 74:1885. <https://doi.org/10.1016/j.camwa.2017.06.053>
16. Dehghan M, Abbaszadeh M (2017) The meshless local collocation method for solving multi-dimensional Cahn-Hilliard, Swift-Hohenberg, and phase-field crystal equations. *Eng Anal Bound Elem* 78:49. <https://doi.org/10.1016/j.enganabound.2017.02.005>
17. Elsey M, Wirth B (2013) A simple and efficient scheme for phase-field crystal simulation. *Math Model Numer Anal* 45:1413. <https://doi.org/10.1051/m2an/2013074>
18. Simeone D, Thorogood GJ, Murphy GL, Forestier A, Garcia P, Luneville L (2019) Radiation-induced micro-structures as ground states of a Swift-Hohenberg energy functional. *J Appl Phys* 125:065103. <https://doi.org/10.1063/1.5072798>
19. Swift J, Hohenberg PC (1977) Hydrodynamic fluctuations at the convective instability. *Phys Rev A* 15:319. <https://doi.org/10.1103/PhysRevA.15.319>
20. Elder KR, Viñals J, Grant M (1992) Ordering dynamics in the two-dimensional Stochastic Swift-Hohenberg Equation. *Phys Rev Lett* 68:3024. <https://doi.org/10.1103/PhysRevLett.68.3024>
21. Hohenberg PC, Swift JB (1995) Metastability in fluctuation-driven first-order transitions: nucleation of lamellar phases. *Phys Rev E* 52:1828. <https://doi.org/10.1103/PhysRevE.52.1828>
22. Velasco MA, Lancheros Y, Garzón-Alvarado DA (2016) Geometric and mechanical properties evaluation of scaffolds for bone tissue applications designing by a reaction-diffusion model and manufactured with a material jetting system. *J Comput Des Eng* 3:385. <https://doi.org/10.1016/j.jcde.2016.06.006>
23. Boyer D, Viñals J (2002) Weakly nonlinear theory of grain-boundary motion in patterns with crystalline symmetry. *Phys Rev Lett* 89:055501–055511. <https://doi.org/10.1103/PhysRevLett.89.055501>
24. Boyer D, Romeu D (2005) Modeling grain boundaries in solids using a combined nonlinear and geometrical method. *Int J Mod Phys B* 19:4047. <https://doi.org/10.1142/S0217979205032607>
25. Boyer D, Vinals J (2001) Domain coarsening of stripe patterns close to onset. *Phys Rev E* 64:050101. <https://doi.org/10.1103/PhysRevE.64.050101>
26. Boyer D (2004) Numerical study of domain coarsening in anisotropic stripe patterns. *Phys Rev E* 69:066111. <https://doi.org/10.1103/PhysRevE.69.066111>
27. Gomez-Solano JR, Boyer D (2007) Coarsening in potential and nonpotential models of oblique stripe patterns. *Phys Rev E* 76:041131. <https://doi.org/10.1103/PhysRevE.76.041131>
28. Burke J, Knobloch E (2007) Snakes and ladders: localized states in the Swift-Hohenberg equation. *Phys Lett A* 360:681. <https://doi.org/10.1016/j.physleta.2006.08.072>
29. Sakaguchi H, Brand HR (1998) Localized patterns for the quintic complex Swift-Hohenberg equation. *Physica D* 117:95. [https://doi.org/10.1016/S0167-2789\(97\)00310-2](https://doi.org/10.1016/S0167-2789(97)00310-2)
30. Hiraoka Y, Ogawa T (2005) Rigorous numerics for localized patterns to the quintic Swift-Hohenberg equation. *Japan J Indust Appl Math* 22:57. <https://doi.org/10.1007/BF03167476>
31. Xiao Q, Gao H (2009) Bifurcation analysis of the Swift-Hohenberg equation with quintic nonlinearity. *Int J Bifurc Chaos Appl Sci Eng* 19:2927. <https://doi.org/10.1142/S0218127409024542>
32. Mohammed WW (2016) Amplitude equation with quantum nonlinearities for the generalized Swift-Hohenberg equation with additive degenerate noise. *Adv Differ Equ* 84:1. <https://doi.org/10.1186/s13662-016-0814-6>
33. Ascher D, Dubois PF, Hinsen K, Hugunin J, Oliphant T (2001) An open-source project: numerical python, University of California USA
34. Ramachandran P, Varoquaux G (2011) Mayavi: 3D visualization of scientific data. *Comput Sci Eng* 13:40. <https://doi.org/10.1109/MCSE.2011.35>
35. Cross MC, Merion D, Yahai Tu (1994) Chaotic domains: a numerical investigation. *Chaos* 4:607. <https://doi.org/10.1063/1.166038>
36. Rabinovich MI, Ezersky AB, Weidman PD (2000) The dynamics of patterns, 1st edn. World Scientific Publishing Co. Pte. Lid, Singapore
37. Morales MA, Fernández-Cervantes I, Agustín-Serrano R, Anzo A, Sampedro MP (2016) Patterns formation in ferrofluids and solid dissolutions using stochastic models with dissipative dynamics. *Eur Phys J B* 89:182. <https://doi.org/10.1140/epjb/e2016-70344-7>
38. Bray A (1994) Theory of phase-ordering kinetics. *J Adv Phys* 43:357. <https://doi.org/10.1080/00018730110117433>
39. Berthier L, Barrat JL, Kurchan J (1999) Response function of coarsening systems. *Eur Phys J B* 11:635. <https://doi.org/10.1007/s100510051192>
40. Jagla EA (2004) Numerical simulations of two-dimensional magnetic domain patterns. *Phys Rev E* 70:046204. <https://doi.org/10.1103/PhysRevE.70.046204>
41. Gelb LD, Gubbins KE (1999) Pore size distributions in porous glasses: a computer simulation study. *Langmuir* 15:305. <https://doi.org/10.1021/la9808418>

42. Bakhshian S, Sahimi M (2016) Computer simulation of the effect of deformation on the morphology and flow properties of porous media. *Phys Rev E* 94:042903. <https://doi.org/10.1103/PhysRevE.94.042903>
43. Bhattacharya S, Gubbins KE (2006) Fast method for computing pore size distributions of model materials. *Langmuir* 22:7726. <https://doi.org/10.1021/la052651k>
44. Tsubota KI, Suzuki Y, Yamada T, Hojo M, Makinouchi A, Adachi T (2009) Computer simulation of trabecular remodeling in the human proximal femur using large-scale voxel FE models: approach to understanding Wolff's law. *J Biomech* 42:1088. <https://doi.org/10.1016/j.jbiomech.2009.02.030>
45. Boyle C, Kim IY (2011) Three-dimensional micro-level computational study of Wolff's law via trabecular bone remodeling in the human proximal femur using design space topology optimization. *J Biomech* 44:935. <https://doi.org/10.1016/j.jbiomech.2010.11.029>
46. Unkovskiy A, Spintzyk S, Brom J, Huettig F, Keutel C (2018) Direct 3D printing of silicone facial prostheses: a preliminary experience in a digital workflow. *J Prosthet Dent* 120:303. <https://doi.org/10.1016/j.prosdent.2017.11.007>
47. Luis E, Pan HM, Sing SL, Bajpai R, Song J, Yeong WY (2020) 3D Direct printing of silicone meniscus implant using a novel heat-cured extrusion-based printer. *Polymers* 12:1031. <https://doi.org/10.3390/polym12051031>
48. Luis E, Pan HM, Bastola AK, Bajpai R, Sing SL, Song J, Yeong WY (2020) 3D printed silicone meniscus implants: influence of the 3D printing process on properties of silicone implants. *Polymers* 12:2136. <https://doi.org/10.3390/polym12092136>
49. Menon A, Póczos B, Feinberg AW, Washburn NR (2019) Optimization of silicone 3D printing with hierarchical machine learning. *3D Print Addit Manuf* 6:181. <https://doi.org/10.1089/3dp.2018.0088>
50. Lee C, Jeong D, Yoon S, Kim J (2020) Porous three-dimensional Scaffold generation for 3D printing. *Mathematics* 8:946. <https://doi.org/10.3390/math8060946>
51. Kuang X, Roach DJ, Wu J, Hamel CM, Ding Z, Wang T, Qi HJ (2019) Advances in 4D printing: materials and applications. *Adv Funct Mater* 29(2):1805290. <https://doi.org/10.1002/adfm.201805290>

Publisher's Note Springer Nature remains neutral with regard to jurisdictional claims in published maps and institutional affiliations.

Springer Nature or its licensor (e.g. a society or other partner) holds exclusive rights to this article under a publishing agreement with the author(s) or other rightsholder(s); author self-archiving of the accepted manuscript version of this article is solely governed by the terms of such publishing agreement and applicable law.

Authors and Affiliations

Marco A. Morales¹  · Sinhue Ruiz-Salgado¹ · Ricardo Agustín-Serrano² · Benito Zenteno-Mateo³ · José I. Rodríguez-Mora³

¹ Facultad de Ingeniería Química, Benemérita Universidad Autónoma de Puebla, Av. San Claudio y 18 Sur C. U. Col. San Manuel, 72570 Puebla, Pue, Mexico

² Facultad de Ciencias Físico Matemáticas, Benemérita Universidad Autónoma de Puebla, Av. San Claudio y 18 Sur C. U. Col. San Manuel, 72570 Puebla, Pue, Mexico

³ Laboratorio de Investigación de Alta Tecnología y Desarrollo de Prototipos y Patentes, Facultad de Ingeniería, Benemérita Universidad Autónoma de Puebla, Av. San Claudio y 18 Sur C. U. Col. San Manuel, 72570 Puebla, Pue, Mexico